Corona-Producing Ice Clouds: A Case Study of a Cold Midlatitude Cirrus Layer

Kenneth Sassen1, Gerald G. Mace1, John Hallett2, and Michael R. Poellot3

1.University of Utah, Salt Lake City, UT
2.Desert Research Institute, Reno, NV
3.University of North Dakota, Grand Forks, ND

Abstract. A high (14.0 km), cold (-71.0ƒC) cirrus cloud was studied by ground-based polarization lidar and millimeter radar, and aircraft probes on the night of 19 April 1994 from the Cloud and Radiation Testbed (CART) site in northern Oklahoma. A rare cirrus cloud lunar corona was generated by this 1-2 km deep cloud, thus providing an opportunity to measure the composition in situ, which had previously only been assumed on the basis of lidar depolarization data and simple diffraction theory for spheres. In this case, corona ring analysis indicated an effective particle diameter of ~22 mm. A variety of in situ data corroborate the approximate ice particle size derived from the passive retrieval method, especially near cloud top where impacted cloud samples show simple solid crystals. The homogeneous freezing of sulfuric acid droplets of stratospheric origin is assumed to be the dominant ice particle nucleation mode acting in corona-producing cirrus clouds. It is speculated that this process results in a previously unrecognized mode of acid-contaminated ice particle growth, and that such small-particle "cold" cirrus clouds are potentially a radiatively distinct type of cloud.

Corresponding author: Kenneth Sassen, 819 W.B. Browning Bldg., University of Utah, Salt Lake City, UT 84112: email- ksassen@atmos.meteor.utah.edu

1. Introduction

It was only recently established, unambiguously, that cirrus clouds composed of nonspherical ice crystals could generate multiple-ring colored corona displays1. Based on an extended period of ground-based polarization lidar measurements, it was shown that, although infrequently observed, a category of midlatitude cirrus clouds in the upper troposphere (UT) appeared to be effective at producing solar or lunar coronas. Their special properties were that the tops of these unusually cold (-60ƒ to -70ƒC) and high (11.5 - 13.4 km) midlatitude cirrus were associated with elevated tropopauses and typically extended into the lowermost stratosphere. Moreover, the cirrus cloud top region generated unusually strong laser backscattering and linear depolarization ratios (d, the ratio of the returned signals in the orthogonal-to-parallel planes of polarization), an indication of an unusual ice crystal shape (and certainly inconsistent with the backscattering behavior of the spherical water droplets usually associated with coronas2). Diffraction and ray tracing theory considerations3 suggest that simple solid ice crystals with comparable length-to-thickness (axial) ratios could satisfy the diffraction and depolarization data constraints, although more complex irregular crystals, aggregates or mixed-phase particles (i.e., melting snowflakes) could also potentially explain this phenomenon4,5. It was inferred that these atypical midlatitude cirrus cloud microphysical conditions were the result of the formation of some characteristic type of ice crystal homogeneously nucleated from stratospheric sulfuric acid droplets.

Up to now, however, the verification of these remote sensing inferences via in situ data intercomparison has been lacking, leaving open the question of the applicability of simple diffraction theory for sizing small nonspherical particles. As shown here, this issue has now been put to the test using a

comprehensive dataset from coordinated remote sensing and aircraft measurements, which sheds new light on the unusual properties of corona-producing cirrus clouds.

2. The Dataset

During April 1994 a special field campaign, the Remote Cloud Sensing Intensive Observation Period (RCS IOP), was conducted at the Department of Energy Atmospheric Radiation Measurement (ARM) Clouds And Radiation Testbed (CART) site near Lamont, OK6. The goal of the RCS IOP experiment was to provide closely coordinated air-truth cloud microphysical data for the testing of remote sensing cloud retrieval algorithms under various atmospheric conditions. On the night of 19 April, an opportunity to study a lunar corona-producing cirrus cloud layer was realized. The instrumentation relied on in this description of the cloud are the University of Utah Polarization Diversity Lidar7 (PDL), the Pennsylvania State University (PSU) W-band radar8, and the University of North Dakota Citation aircraft. Supplemental information is provided by the three-hourly IOP schedule of CART radiosonde releases and other archived information.

The Citation mission over the 0110-0413 (all times are UTC) period was designed to closely support the ground-based remote sensing observations, with updates on the properties of the cloud layer based on real-time lidar data conveyed to the Citation scientist via ground-to-air communications from the PDL van. In this case, the mission consisted of a series of constant-level legs centered above the CART site first ascending and then descending through the cloud at ~300 m height intervals. The legs averaged ~40 km in length and were performed along the flight leg-level winds. The in situ instrumentation relied on here to describe cloud content are the standard PMS Forward Scattering Spectrometer Probe (FSSP-100) and two-dimensional crystal (2D-C) probes, and two devices from the Desert Research Institute, a Formvar replicator9 and the new Cloudscope device. The latter two instruments collect ice crystals by impaction to either create permanent plastic replicas, or record their magnified shapes on video imagery, respectively.

It should be noted that the 2D-C probe on this occasion collected only concentration data (for particles greater than the ~35 mm diameter detection threshold) because of a data recording problem. This "shadow/or" data includes all particles large enough to trigger the probe, including those that would appear as "zero-area" images. Because of optical effects and the response of the electronics, the sample volume of these optical array probes depends both on the size and velocity of the particles passing through the sampling beam, particularly for small particles ($<$~150 mm). As particles become smaller and velocities greater, the particles must pass closer to the center of focus of the beam in order to be detected, giving a smaller effective sample volume. When the particle sizes are known from the image data, corrections can be applied to account for particle size and velocity10. Although we do not attempt any corrections in this study because these data do not contain sizing information, it should be pointed out that the reported 2D-C particle concentrations (sampled at 120 m s-1) are likely to be significantly underestimated; for example, for particles of 100 mm and 50 mm diameter, the uncorrected concentrations given here should be multiplied by factors of 2.7 and 31.9, respectively. Also note that although the FSSP probe is normally intended for use in water droplet clouds, under conditions in which the contamination from relatively large and numerous ice crystals are absent, this probe provides reasonably accurate small ice crystal concentrations and sizes11. The FSSP data were collected in 15 size bins with minimum and maximum sizes of 2.8 mm and 54.2 mm, accounting for aircraft speed effects.

3. The Upper-Tropospheric Environment

The moisture in the UT that generated the cirrus observed during the early UTC hours of 19 April 1994 can be traced back in time to an extensive stream of moisture that had origins over the tropical eastern Pacific Ocean. The associated cirrus clouds are visible in the GOES 7 satellite imagery from 17 April (Fig. 1a) extending from the northern Baja area southwestward along a subtropical jet stream. This cloud system moved rapidly into the four-corners region of the Desert Southwest in association with a deepening UT disturbance. Although the disturbance weakened on 18 April, satellite imagery still shows cirrus streaming eastward into New Mexico (Fig. 1b). As shown below, tenuous cirrus clouds were first observed by the lidar in northcentral Oklahoma at a height of ~14 km beginning at ~0200 on 19 April. The satellite imagery

at 0230 (Fig. 1c) shows the eastward advection of mesoscale regions of thicker cirrus indicated by the colder infrared brightness temperatures. The movement of these cirrus are associated with the deepening of the layer subsequently observed by the lidar and radar.

The evolution and structure of the cirrus clouds observed at the CART site can be partially understood by examining the thermodynamic soundings observed in the radiosondes. As shown in Fig. 2a, the sounding launched at 0230 on 19 April displays an interesting thermal stratification. The primary feature of the potential temperature profile is the layer bounded by the tropopause near 13.8 km and the inversion at 12.2 km. Between 12.5 and 13.0 km, the layer lapse rate is 9.4 K km-1, which is conditionally stable with respect to the ice pseudoadiabatic process. Earlier soundings at 2130 and 2330 on 18 April (not shown) also showed this layer of conditional stability, which indicates that cirrus cloud development could be aided by convective processes once formation takes place. Figure 2b provides profiles of wind speed and direction, revealing the presence of a weak (~25 ms-1) subtropical jet corresponding to the conditionally stable layer.
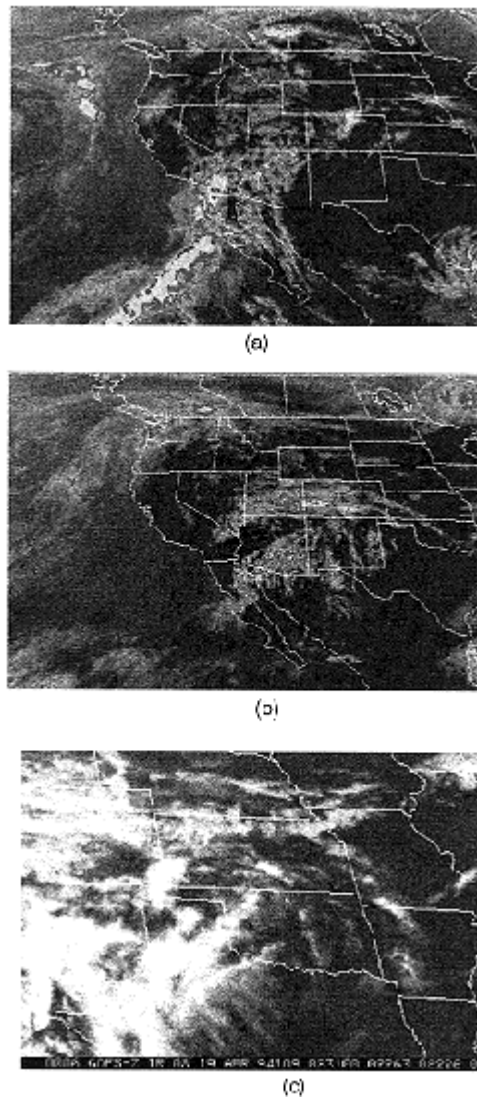

(a)

(b)

(c)

Figure 1. GOES 7 satellite imagery showing the evolution of the cirrus event observed at the CART site at (a) 1800 UTC 17 April 1994, (b) 1800 18 April 1994, and (c) 0230 19 April 1994. Note that the shading scheme used in (c) is different than in (a) and (b), and that the location of the CART site is marked by a dot in north-central OK.
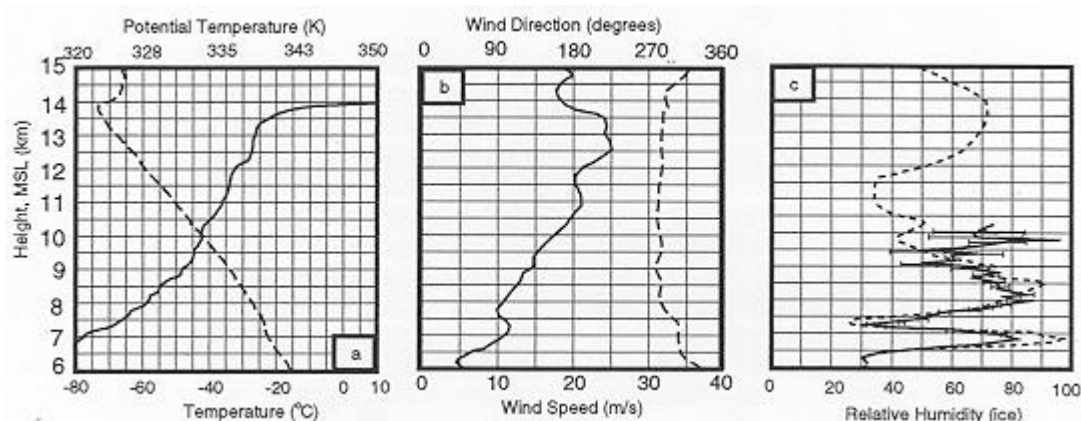
Figure 2. Thermodynamic sounding collected by a radiosonde launched at 0230 19 April 1994, showing (a) temperature (dashed) and potential temperature, (b) wind speed (dashed) and direction, and (c) relative humidity (dashed, in percent with respect to ice) compared with a 2-h average of data from of a water vapor Raman lidar (courtesy of S. H. Melfi).

Although radiosonde-measured relative humidity is known to be subject to large uncertainties in the UT, we show in Fig. 2c that the 0230 sounding is at least indicative of the trend of moisture with height. Compared with the sounding profiles is a 2-h (0300 - 0500) average of relative humidity (RHI, with respect to ice) derived from the NASA Goddard Space Flight Center water vapor Raman lidar system. (The long time average is needed to obtain reliable data from the comparatively dry UT- note the error bars increasing with height.) The radiosonde profile reveals a local maximum of moisture centered near the tropopause associated with the cirrus observed within the unstable layer, a dry layer between 11 - 12 km, and highly layered moisture structures below 10 km. Local maxima near 90 and 95% RHI are observed near 8.5 and 7.0 km, respectively. Earlier soundings showed much lower humidities in the upper layer prior to the appearance of the cirrus locally. Note that the Raman lidar profile begins an increasing trend at ~-40fC, which is not reflected in the radiosonde data because of well known problems with the humidity sensing elements.

4. Remote Sensing Cloud Displays

Given in Fig. 3 are height versus time displays of PDL backscattering (in relative units based on a
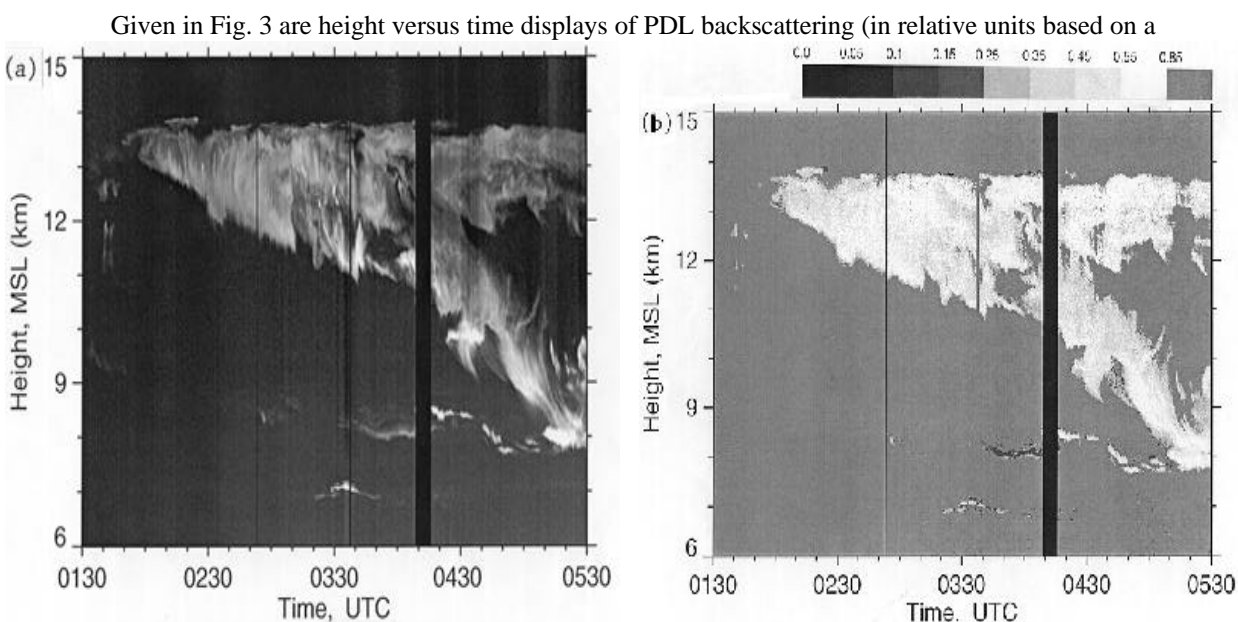
Figure 3. Time-height displays of lidar (a) backscattering (in arbitrary units) and (b) linear depolarization ratios (see key at top) from the cirruscloud layer studied on 19 April from the Southern Great Plains CART site.

logarithmic grayscale) and linear depolarization ratios (see d value key at top) over most of the period of the passage of the cirrus cloud mass. These high resolution PDL data were collected at 1-s time and 6-m height resolutions in the 0.532 um wavelength channels. Note that the duration of the Citation mission within the cirrus layer lasted from 0200 - 0340, showing that the sampling occurred as the cirrus layer gradually thickened from ~1.0 to 2.0 km in depth, but prior to the significant vertical development that took place from 0400-0530. The injection of the particles at ~0400 lasted only briefly, but no corona were noted subsequently, probably because of multiple scattering activity in the more vertically-developed cloud.
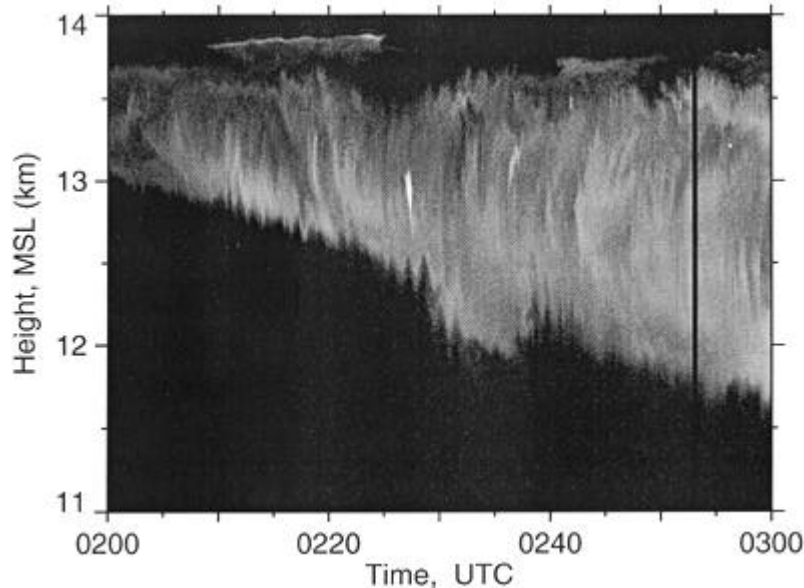

Figure 4. Expanded PDL relative returned energy display of the cirrus layer, corresponding to the aircraft mission, showing 6-m by 1-s resolutiondetails of cloud generating features and, as the brightest streaks, contrails from the Citation.

The lidar d-value display (Fig. 3b) reveals the expected depolarization pattern of a corona-producing cirrus layer1. The upper cloud region in contact with the tropopause frequently generates the characteristically high 0.5-0.8 d values, while the depolarization ratios below tend to assume the 0.4-0.5 values more typical of cirrus clouds4. Since cirrus particle generation probably occurred principally at or near cloud top, this depolarization trend reflects changes in the evolving ice crystal habit or axial ratio with increasing fallspeed and ventilation. An expanded view of the upper cirrus cloud region during that part of the aircraft mission considered here is shown in Fig. 4, where the upper cloud layer is seen to be composed of fallstreaks from numerous cloud-top generating cells. Since the sounding data (Fig. 2a) indicate a tropopause height of 13.8 km, many generating cells are located at the tropopause: some more elevated cloud patches lie in the lowermost stratosphere. Also note that the three bright cloud features embedded within the cirrus correspond to the contrails produced by the Citation during the performance of the racetrack patterns, as tracked visually from the CART site.

The PSU radar reflectivity factor display in Fig. 5 reveals that the tropopause-topped cirrus layer almost escaped radar detection; only the deep precipitation streamer was effectively sampled even at the relatively short 3.2-mm wavelength. Due to the significant differences in the scattering of light waves and microwaves by ice particle clouds, this data comparison can be treated as a proxy indicator of particle size. Since the upper portion of the layer, which amply scattered visible laser energy, remained well below the detection threshold of the radar (with the exception of a brief interval near 0340), it must have been composed of particles too small to be detected by the radar. Only as the base of the layer descended

through 10.5 km after 0400 did the radar detect the higher reflectivities (see key at top) associated with larger ice crystals.
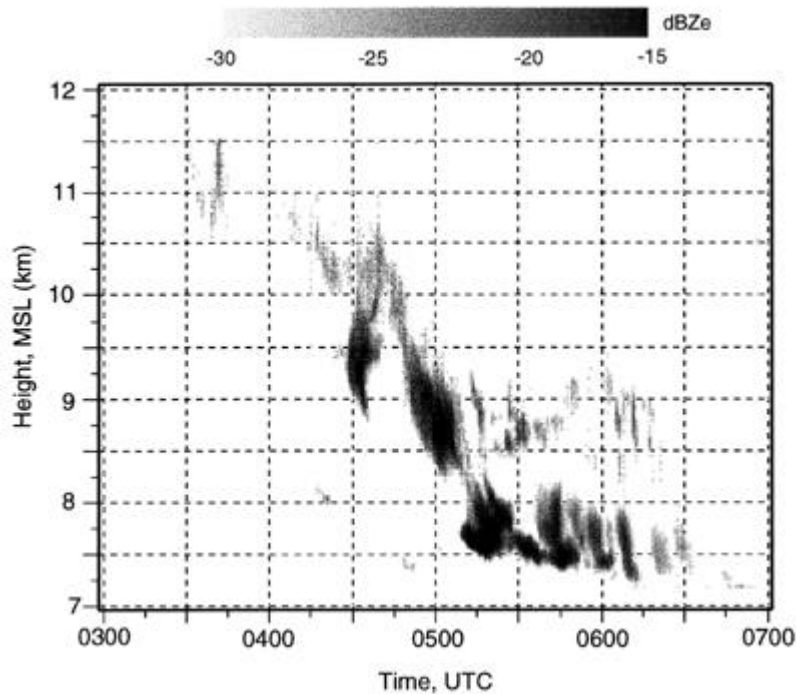

Figure 5. Time-height cross section of radar reflectivity factors (see key at top) observed by the PSU 94 GHz cloud radar on the night of 19 April 1994. Like the lidar, the radar was pointing vertically during this period.

We note that the appearance of this cloud is similar to that described in an earlier well documented jet stream cirrus case study[5], although the dynamics of this situation are quite different. What the two cloud systems appear to have in common are indications that the vertical cloud development occurred in response to a period of active precipitation from a tropopause-topped layer that was successful in penetrating a dry subcloud region (see Fig. 2c). The larger crystals that remained after sedimenting through the dry layer near 11.0 km appear to have resulted in the rapid destabilization and ice generation in the higher humidity layers below 10 km.

5. Corona Analysis

The lunar corona was variably recorded in the PDL operator field notes over the period of aircraft operations. Although a few attempts were made to photograph the corona, only the example shown in Fig. 6 obtained at 0351 proved suitable for analysis. This photograph was taken with a 35-mm camera and a 55-mm lens, using a ~3-min exposure (note the star streaks). Employing the same manual analysis technique used earlier[1], the angular separation q between the centers of the moon and the first corona red band was determined to be $1.5f$; the angle of second red band, which is indistinct in the photograph, was estimated at $2.9f$. These angles are converted to a measure of the mean particle diameter d with the use of the relation d = l (n + 0.22) / sin q, where n is the order of the red band, and a wavelength l = 0.49 mm was chosen in accordance with Mie theory corona colorization findings[1,2]. The derived particle diameter of ~22 mm is consistent with the upper range of earlier measurements of cirrus cloud coronas[1].

6. In Situ Findings

The above evidence conforms with our previous understanding of the conditions under which cirrus cloud coronas form-- they occur at the tropopause in unusually high and cold cirrus layers (for

Figure 6. Time (~3-min) exposure of a lunar corona obtained at 0351 UTC on 19 April 1994 during a coordinated aircraft and ground-basedremote sensing study of a cold cirrus cloud layer over Oklahoma.

midlatitudes), generate atypically high lidar depolarization indicative of some uncommon crystal shape, and would appear to be composed of 20 - 30 mm diameter particles1. In this section we examine the in situ data provided by the Citation platform to assess the validity of these remote sensing deductions.

In Fig. 7 is shown vertical (10-m average) profiles of temperature and ozone to describe the environment of the upper troposphere and set the stage for the characterization of the cirrus cloud. Since the profiles for the descending series of aircraft legs are similar to those from the ascending legs, only the latter are shown for clarity. The in situ ozone profile demonstrates that the aircraft did not penetrate the
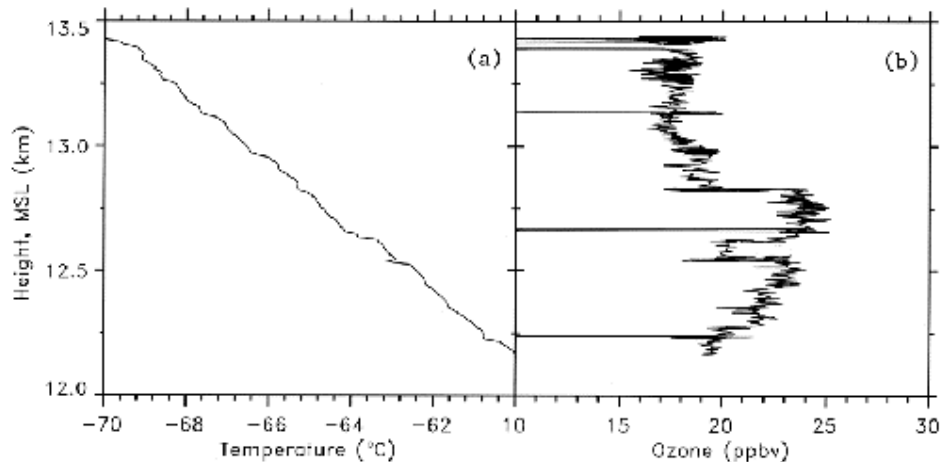

Figure 7. In situ data from the ascent portion of the Citation flight on 19 April, showing 10-m height averaged (a) ambient temperature and (b)ozone concentration (in parts per billion by volume). The abrupt ozone decreases are part of a calibration procedure.

tropopause, since an abrupt increasing trend marking the troposphere/stratosphere boundary was not observed (see Ref. 5). However, according to the CART sounding data, the aircraft ceiling altitude of nearly 13.5 km came close to the 13.8 km tropopause level. On the other hand, it is interesting to note the abrupt drops in ozone concentration between 12.5 - 12.6 and at 12.8 km, for, as shown below, these heights correspond closely to the cirrus cloud boundaries measured by the Citation.
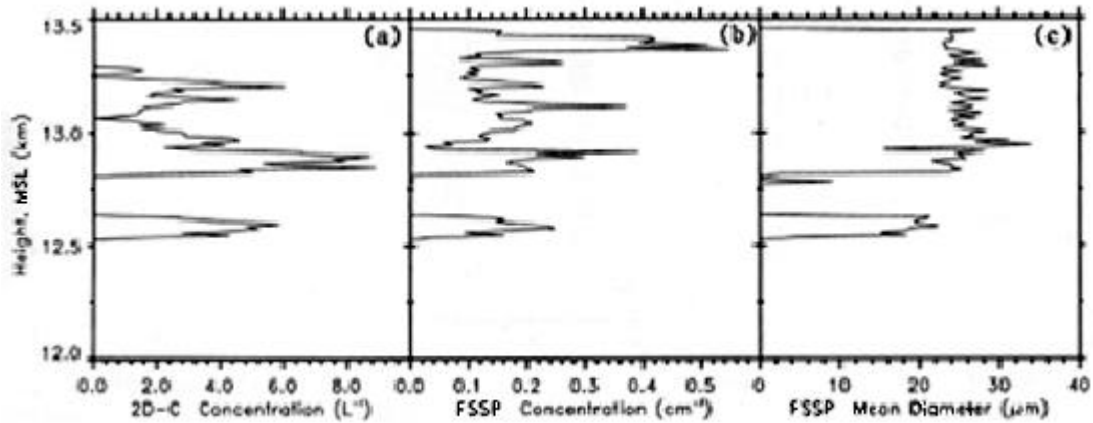
Figure 8. As in Fig. 6, except for (a) 2D-C probe shadow/or and (b) FSSP particle concentrations (note differences in units), and (c) FSSP mean particle diameters.
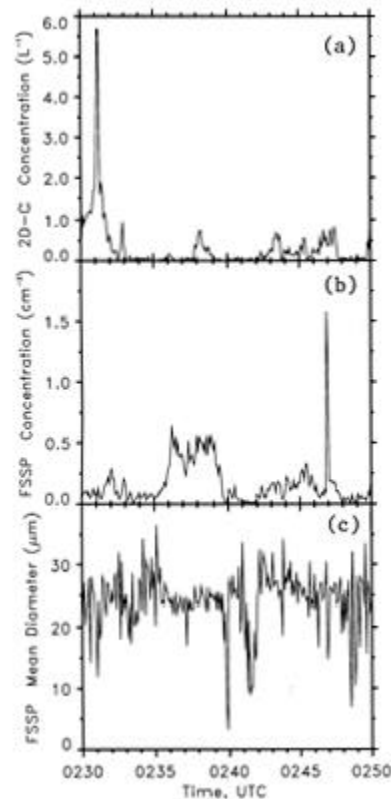

Figure 9. Aircraft data from an extended leg quite close to the cirrus cloud top (13.39 km), showing (a) 2D-C shadow/or and (b) FSSP particle concentrations, and (c) FSSP mean particle diameters as a function of time.

Figure 8 provides the corresponding particle concentrations from the FSSP and 2D-C probes, along with the FSSP-derived mean particle diameter. It can be seen that the uncorrected 2D-C counts (for particles >~35 mm diameter) range from a few to several per liter and approach zero near the cloud top region. Thus, the FSSP data should be especially trustworthy near the cloud top, as we further explore in Fig. 9. Here is depicted 5-s average data from an extended leg performed at the aircraft ceiling altitude from 0230 - 0250, at an average height of 13.39 km and temperature of -69.8ƒC. With FSSP mean diameters varying between 20 - 30 mm, it is not surprising that the detected 2D-C particle concentrations generally do not exceed 1.0 L-1. Note that from 0236:35 - 0237:05 (between heights of 13.35 - 13.40 km), for example, 2D-C counts almost disappear while FSSP mean particle concentrations exceed 500 L-1. With

this data being particularly reliable, Fig. 10 shows the measured FSSP ice particle size spectrum, which has been fitted with the inserted gamma size distribution. This reveals a mean diameter of 23 mm at a total concentration of 438 L-1. Still higher FSSP concentrations (with a remarkable 1-s peak of 3,350 L-1) occur at 0246:45, but this corresponds to the Citation briefly sampling one of its own contrails (as shown in Fig. 4). Such high concentrations of minute (~15 mm) particles are typical of young contrails12. The vertical velocity data for the cloud-top leg (not shown) frequently indicate upward motions of ~0.5 - 1.0 m s-1, which shows this to be a region of active particle generation, but also reveal a considerable amount of up- and down-draft structure on a scale of a few kilometers that accounts for the cellularity observed by the lidar (Fig. 4).

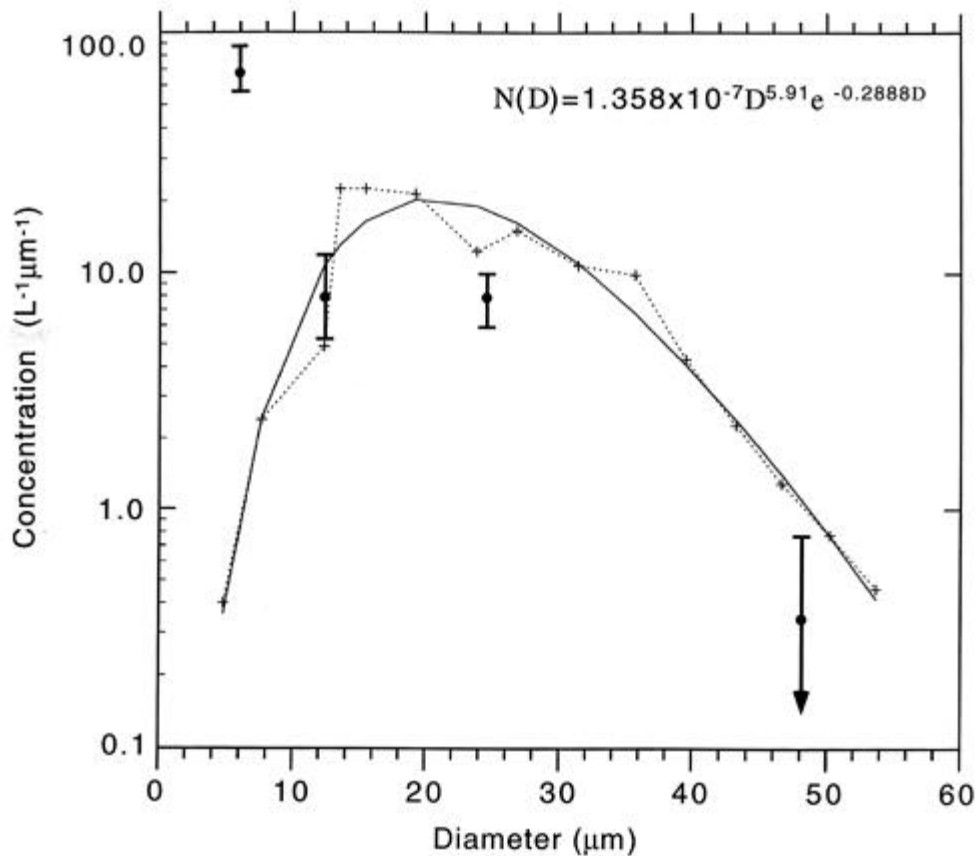$$N(D)=1.358 \times 10^{-7}D^{5.91}e^{-0.2888D}$$

Figure 10. A 30-s average FSSP particle size distribution (dashed line) fitted with the inserted gamma distribution, obtained near cloud top from 0236:35 - 0237:05 when no 2D-C counts were measured. The data points with error bars represent an analysis of Cloudscope data for a 5-s period starting at 0236:05

As for the direct measurement of the microphysical content of the cloud, we rely on both the Cloudscope and Formvar replicator devices. Each instrument has its advantages and drawbacks under the harsh environmental conditions encountered during the aircraft mission. For example, although the Cloudscope is a new device still undergoing evaluation and does not produce very detailed images of small ice particles, the video images can be electronically processed to obtain particle size distributions. A typical image obtained at 0237:06 (corresponding to the period of Fig. 10) is given in Fig. 11, where the particles identified as "new" were impacted on the window since the last frame was collected. The particle sizes range from about 3 mm, the approximate particle collection threshold, to 35 mm. The results of an analysis of 18 such samples is provided in Fig. 12, where the particle size distributions, as expressed in five bins with average maximum dimensions of 6, 12, 24, 48, and 80 mm, are shown as a function of time. Note the tendency for bimodal distributions with a peak in the expected ~20 - 25 mm size range especially at ~0235 and 0250, and the usual absence of particles >64 mm. The size distribution collected at 0236:05 is included
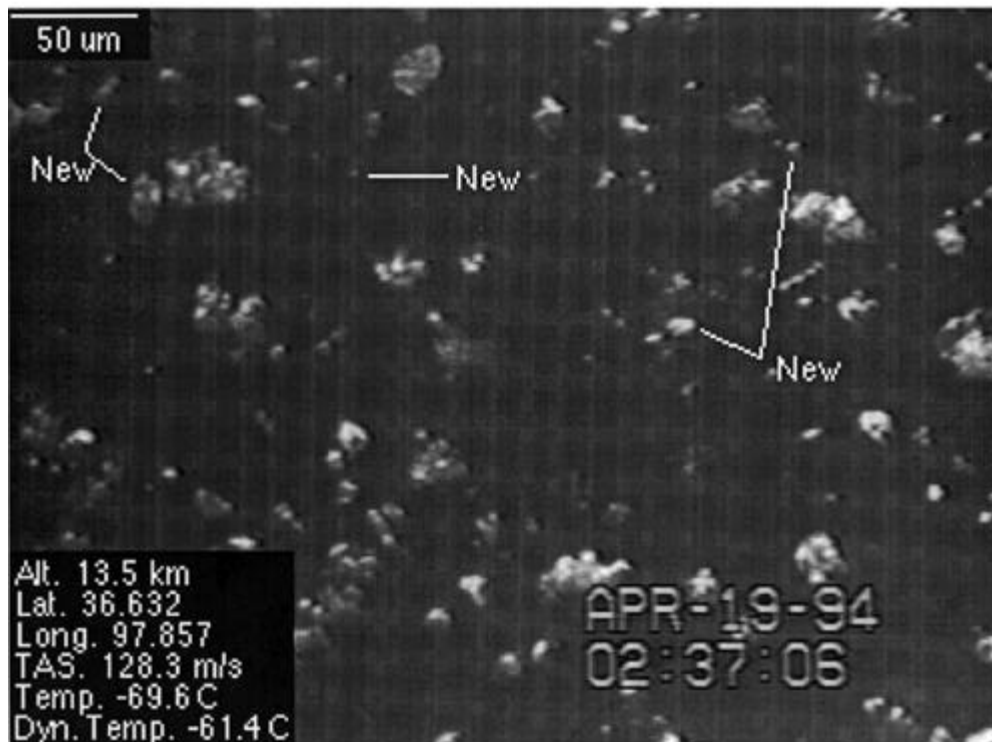
Figure 11. Typical video Cloudscope image of impacted ice particles collected under the indicated conditions. Note the preponderance of ~25 mm particles.
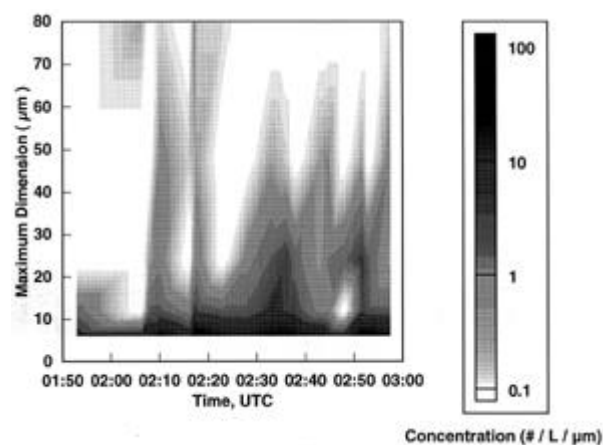

Figure 12. A synopsis of Cloudscope observations of particle size distributions as the aircraft ascended through the cirrus cloud layers.

in Fig. 10 for comparison with the FSSP data. The agreement between the two vastly dissimilar probing methods is reasonable.

The replicator device performed erratically during the experiment, probably because of the effects of the frigid temperatures on the replicating solution, but fortunately obtained detailed casts of the ice crystals present at several locations. Shown in Fig. 13 are photomicrographic montages of ice particles collected at 0210 near cloud base (12.6 km) and at 0236:30 near cloud top (13.4 km). Both cloud samples appear to be unusual with regard to previously studied midlatitude cirrus clouds at warmer temperatures, where hollow crystals and bullet rosettes seem to dominate13. The sample (a) obtained in the lower cloud contains obvious solid column crystals, and also more complex particles that, although shattered by the
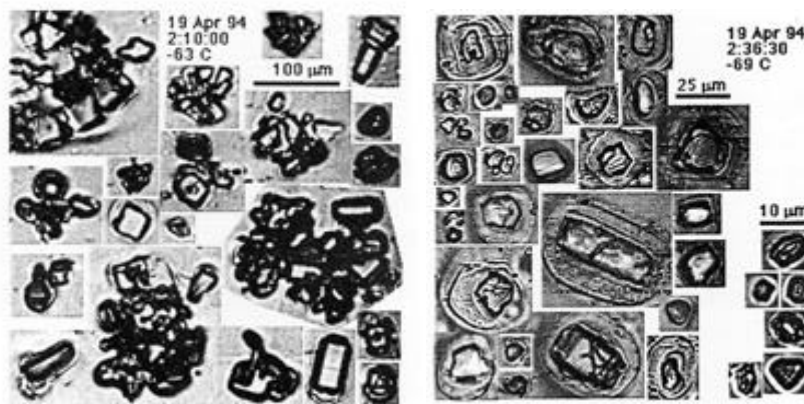
Figure 13. Examples of Formvar-preserved ice particle collected near (a) cloud base and (b) cloud top at the indicated times and temperatureson 19 April. Note the inserted scales in microns.

impact, are recognizable as polycrystalline particles composed of plates and columns. The largest of these particles, which were detected by the 2D-C probe at a concentration of ~5 L-1, may represent particle aggregates.

Finally, the images of the ice particles from the upper cloud region (Fig. 13b), which probably had the greatest impact on corona generation1, appear to be rather odd. They resemble simple plates and columns ranging from 5 to 40 mm in maximum dimension, but they lack the sharp edges and facets proving the presence of a hexagonal symmetry. Such particles, along with the unusual small square and triangular particle shapes in Fig. 13a, may signify the influence of acid contamination on ice particle shape. The character of the Formvar film coating the particles appears adequate to have properly preserved the crystals, and although particle sublimation effects could have produced such rounded shapes, this explanation is inconsistent with the indicated new particle generation within the cloud-top convective cells.

7. Summary and Conclusions

A coherent picture with respect to earlier ground-based research1 of the physical properties and microphysical content of a corona-producing cirrus cloud has emerged from this aircraft-supported case study. For the first time, agreement between passively-sensed (i.e., photographic) and in situ-measured mean ice particle sizes has been achieved through coordinated aircraft observations. The effective ice particle size of ~22 mm deduced from corona photograph analysis is in good agreement with the ~25 mm mean diameters measured by the FSSP in the absence of the contamination from the far fewer, larger ice crystals. We consider this a validation of the passive particle size retrieval method in the sense that independent measurement approaches, each with their limitations and uncertainties, have come into reasonable compliance.

Also for the first time, direct particle capture and microscopic examination has yielded valuable clues regarding the nature of the small corona-producing particles that also tend to generate unusually strong laser depolarization. Although previous experimental and theoretical studies4 have indicated that the high d values could be due either to certain simple, solid, hexagonal particle shapes like short columns, or, paradoxically, to particles exhibiting complex surface structures like partially melted or aggregated particles, the particles captured in the upper cloud region cannot be easily classified. This suggests that unique particle shapes may inhabit regions of corona-producing cirrus clouds.

The cause of this crystal growth phenomenon is likely linked to the ice crystal nucleation mechanism, wherein aqueous droplets of stratospheric sulfuric acid freeze homogeneously as they become diluted during growth from water vapor upwelling from the troposphere. The stratosphere has long been known to photochemically generate sulfuric acid droplets14, even without the intervention of explosive volcanic eruptions, but more recent research has addressed the fate of these particles in the

troposphere[5,9,15]. Upon approaching or crossing the tropopause through a number of exchange processes[15], the sulfuric acid droplets can either absorb ammonia gas to become neutralized into ammonium sulfate crystals (an abundant and active cloud forming nuclei), or they can grow from water vapor absorption until homogeneous freezing occurs. Since sulfuric acid is apparently not incorporated into the lattice of frozen water, it is extruded during freezing to coat the ice particles, presumably leading to the ice particle types shown here by interfering with the deposition of water vapor on the ice surface. In effect, this represents a new mode of tropospheric ice particle growth, which may have important consequences ranging from the heterogeneous chemistry of ozone depletion[16] to the influence of high cirrus clouds on the radiative equilibrium that controls our climate, as well as optical displays.

It is significant that this category of small particle-containing, "cold" cirrus is in such sharp contrast to the composition of the "cirrostratus" cloud models that remains in vogue in climate simulations. The latter type of cloud content model is based on seemingly typical in situ measurements using probes generally insensitive to minute particles, and certainty do not deal with the type of high, cold, and most difficult to sample cirrus cloud considered here. Not only are the size distributions dissimilar, but a contrast exists in particle shapes-- radial hexagonal crystals versus simple uniaxial particles. Although a wide variety of cirrus cloud contents are likely to be found globally, fundamental differences may exist in the radiative properties of these two obviously dissimilar cirrus cloud models, particularly with regard to the balance between the solar and infrared radiative components that helps determine the heating rate of the earth/atmosphere system.

Acknowledgments.

References

1. K. Sassen, "Corona producing cirrus cloud properties derived from polarization lidar and photographic analyses", Appl. Opt. 30, 3421-3428 (1991).

2. J. A. Lock and L. Yang, "Mie theory of the corona", Appl. Opt. 30, 3408-3414 (1991).

3. Y. Takano and K. N. Liou, "Solar radiative transfer in cirrus clouds. Part I: Single-scattering and optical properties of hexagonal ice crystals", J. Atmos. Sci. 46, 3-19 (1989).

4. K. Sassen, "The polarization lidar technique for cloud research: A review and current assessment", Bull. Amer. Meteor. Soc. 72, 1848-1866 (1991).

5. K. Sassen, D. O'C. Starr, G. G. Mace, M. R. Poellot, S. H. Melfi, W. L. Eberhard, J. D. Spinhirne, E. W. Eloranta, D. E. Hagen and J. Hallett, "The 5-6 December 1991 FIRE IFO II jet stream cirrus case study: Possible influences of volcanic aerosols", J. Atmos. Sci. 52, 97-123 (1995).

6. G. M. Stokes and S. E. Schwartz, "The Atmospheric Radiation Measurement (ARM) program: Programmatic background and design of the cloud and radiation testbed", Bull. Amer. Meteor. Soc. 75, 1201-1221 (1994).

7. K. Sassen, "Advances in polarization diversity lidar for cloud remote sensing", Proc. IEEE 82, 1907-1914 (1994).

8. E. E. Clothiaux, M. A. Miller, B. A. Albrecht, T. P. Ackerman, J Verlinde, D. M Babb, R. M. Peters, and W. J. Syrett, "An evaluation of a 94 GHz radar for remote sensing of cloud properties", J. Atmos. Oceanic. Technol., 12, 201-229 (1995).

9. W. P. Arnott, Y. Y, Dong, and J. Hallett, "Role of small ice crystals in radiative properties of cirrus: A case study, FIRE II, November 22. 1991", J. Geophys. Res. 99, 1371-1381 (1994).

10. D. Baumgardner and A. Korolev, "Airspeed Corrections for Optical Array Probe Sample Volumes", J. Atmos. Ocean. Technol. 14, 1224-1229 (1997).

11. J.-F. Gayet, G. Febvre, and H. Larson, "The reliability of the PMS FSSP in the presence of small ice crystals", J. Atmos. Ocean. Tech. 13, 1300-1310 (1996).

12.K. Sassen, "Contrail-cirrus and their potential for regional climate change", Bull. Amer. Meteor. Soc. 78, 1885-1903.

13.K. Sassen, N. C. Knight, Y. Takano, and A. J. Heymsfield, "Effects of ice crystal structure on halo formation: Cirrus cloud experimental and ray-tracing modeling studies", Appl. Opt. 30, 4590-4601 (1994).

14.C. E. Junge, C. W. Chagnon, and J. E. Manson, "Stratospheric aerosols", J. Meteor. 18, 81-110 (1961).

15.P. Hamill, E. J. Jensen, P. B. Russell, and J. J. Bauman, "The life cycle of stratospheric aerosol particles", Bull. Amer. Meteor. Soc. 78, 1395-1410.

16.J. Reichardt, A. Ansmann, M. Serwazi, C. Weitkamp, and W. Michaelis, "Unexpectedly low ozone concentrations in midlatitude tropospheric ice clouds: A case study", Geophys. Res. Lett. 23, 1929-1932.